*Article*

# Large-Scale Preparation of Ultrathin Bimetallic Nickel Iron Sulfides Branch Nanoflake Arrays for Enhanced Hydrogen Evolution Reaction

Shengjue Deng [1,†], Changsheng Liu [1,†], Yan Zhang [1,*], Yingxi Ji [1], Bingbao Mei [2,*], Zhendong Yao [3] and Shiwei Lin [1,*]

[1] State Key Laboratory of Marine Resource Utilization in South China Sea,
  Department of Materials Science and Engineering, Hainan University, Haikou 570228, China
[2] Shanghai Synchrotron Radiation Facility, Shanghai Advanced Research Institute,
  Chinese Academy of Sciences, Shanghai 201800, China
[3] College of Materials and Chemistry, China Jiliang University, Hangzhou 310018, China
* Correspondence: zyan@hainanu.edu.cn (Y.Z.); meibb@sari.ac.cn (B.M.); linsw@hainanu.edu.cn (S.L.)
† These authors contributed equally to this work.

**Abstract:** Developing the large-scale preparation of non-noble metal catalysts with high performance is crucial for promoting the electrochemical production of hydrogen from water. In this work, a novel $TiO_2@FeNi_2S_4$ ($TiO_2@FNS$) branch nanoflake array on Ni foam can be prepared at a large scale (50 cm$^2$) by combining an atomic-layer-deposited (ALD) $TiO_2$ skeleton with one-step facile low-temperature (<100 °C) sulfurization method. As-prepared $TiO_2@FNS$ arrays exhibit excellent hydrogen evolution reaction (HER) performance with an overpotential of 97 mV at 10 mA cm$^{-2}$, superior to the FNS counterpart (without $TiO_2$ coating) and other reported catalysts. The enhanced HER catalytic performance of $TiO_2@FNS$ is attributed to the increased specific surface area and improved structural stability due to the introduction of $TiO_2$ coating. Moreover, theoretical calculations also show that the bimetallic NFS structure is more favorable to the dissociation of water molecule and the desorption of H than the monometallic $Ni_3S_2$ counterpart. With the combination of experimental results and theoretical calculations, this work has enlightened a new way of exploring high-efficient catalysts for HER.

**Keywords:** $FeNi_2S_4$; $TiO_2$; branch nanoflake arrays; electrocatalyst; hydrogen evolution reaction

## 1. Introduction

Electrocatalytic hydrogen evolution reaction (HER) by water splitting is a green and promising technology to generate hydrogen with high purity and high yield [1–3]. During the whole HER process, the electrocatalyst plays a key role in hydrogen production [4–6]. The perfect electrocatalyst should possess facile synthesis process for large-scale application, cheap raw materials to cut cost, and outstanding electrochemical performance for increasing $H_2$ production [7,8]. Currently, Pt and Pt-based alloys present the best HER performance compared with other catalysts, however, the high price, low crustal abundance and inferior long-term cycle stability impede their widespread application [9]. Based on these scientific challenges, a variety of highly efficient non-noble metal catalysts (such as transition metal oxides [10], sulfides [11,12], selenide [13,14], nitrides [15], carbide [16], and phosphide [17], etc.) have been designed and synthesized by researchers.

Among these non-precious electrocatalysts, transition metal sulfides are expected to be the candidates for replacing the Pt-based catalysts due to their low cost, facile preparation and good stability [18]. Moreover, the HER activity of these metal sulfides can be further improved through introducing other metal species to form binary metal sulfides [19]. In addition, the traditional powder electrode materials are always subject to unsatisfied catalytic activity because the insulating binder used in the electrode preparation process

leads to inferior contact between the electrode and electrolyte [20]. Therefore, constructing integrated binary metal sulfides electrode is an efficient strategy to realize satisfied HER performance. For example, Sivanan-tham et al. [21] designed in situ grown $NiCo_2S_4$ nanowire array on Ni foam with a two-step method to form an integrated electrode. With an enlarged specific surface area, the fabricated $NiCo_2S_4$ nanowire array displayed a better HER activity than $NiCo_2S_4$ nanoparticles. However, most reported binary metal sulfides have no obvious morphology change before and after sulfurization process [22–24], which fails to further increase the specific surface area and expose active sites to optimize HER performance. Moreover, improving the structural stability of binary metal sulfides to meet the practical application requirement still remains a great challenge.

In this work, we report a simple atomic-layer-deposition (ALD) and sulfurization strategy to rationally construct integrated $TiO_2@ FeNi_2S_4$ ($TiO_2$@FNS) arrays as robust electrocatalysts for HER in alkaline medium. The ALD fabricated $TiO_2$ coating not only enhances the structural stability of final $TiO_2$@FNS arrays, but also leads to the formation of unique branch nanoflakes morphology. Therefore, the binder-free $TiO_2$@FNS arrays possess large specific area and strong adhesion on the Ni foam, endowing them with more active cites, faster ions/electrons transport rate and better structural stability. In alkaline medium, the $TiO_2$@FNS branch nanoflake arrays could deliver a better HER property than the FNS (without $TiO_2$ coating) counterpart with a lower overpotential of 97 mV at 10 mA $cm^{-2}$. Furthermore, excellent durability is demonstrated when using the $TiO_2$@FNS arrays as electrocatalyst. More importantly, density functional theory (DFT) calculations revealed that $FeNi_2S_4$ shows larger $H_2O$ absorption energy ($-0.13$ eV) and smaller $H^*$ desorption energy (0.82 eV) than those of monometallic $Ni_3S_2$ ($-0.09$ eV/1.01 eV), thus leading to the better HER performance of $FeNi_2S_4$ in alkaline solution. Our work can provide a reference for the rational design of efficiently integrated arrays for applications in electrocatalysis and energy storage.

## 2. Results and Discussion

### 2.1. Morphology and Structure Analyses

The preparation process of integrated $TiO_2$@FNS arrays is schematically illustrated in Figure 1. Firstly, the $Fe_2Ni_2CO_3(OH)_8$ (FNC) nanosheet precursor on nickel foam is fabricated via a facile hydrothermal process with $Fe(NO_3)_2$ as the Fe resource. Especially, $Fe^{2+}$ ions react with $Ni^{2+}$ ions provided by Ni foam substrate to form the final FNC nanosheet arrays. Afterward, an ALD method is used to construct a uniform $TiO_2$ coating on the surface of FNC nanosheet ($TiO_2$@FNC). After a simple low-temperature sulfurization process, the $TiO_2$@FNC is converted to final $TiO_2$@FNS branch nanoflake arrays.



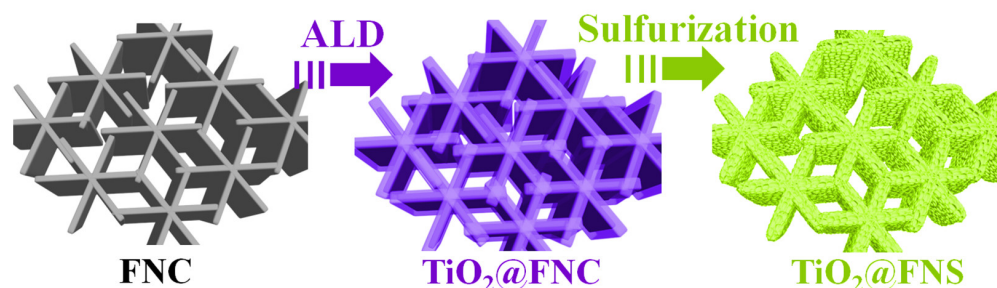**Figure 1.** Schematic illustration of the preparation process for binder-free $TiO_2$@FNS arrays.

The morphology change in different samples can be observed by their scanning electron microscope (SEM) images (Figure 2). The large FNC nanosheets with thickness of 30–60 nm are developed vertically on the surface of Ni foam substrate, forming a three-dimensional porous and open structure (Figure 2a,d). With a $TiO_2$ coating, the thickness of the $TiO_2$@FNC nanosheet increases to 40~70 nm, and the porous network structure is still perfectly preserved (Figure 2b,e), suggesting that the ALD process has no effect on the morphology structure. Different from the $TiO_2$@FNC, the morphology of final $TiO_2$@FNS

arrays changed radically after the final sulfurization in $Na_2S$ solution at 90 °C. Obviously, numerous small nanoflakes are distributed on the outer layer to form a novel $TiO_2$@FNS branch nanoflake arrays structure (Figure 2c,f). Moreover, the $TiO_2$@FNS sample is ~50 $cm^2$ with black color (the inset in Figure 2f), indicating our preparation process can be easily adapted for large-scale production.
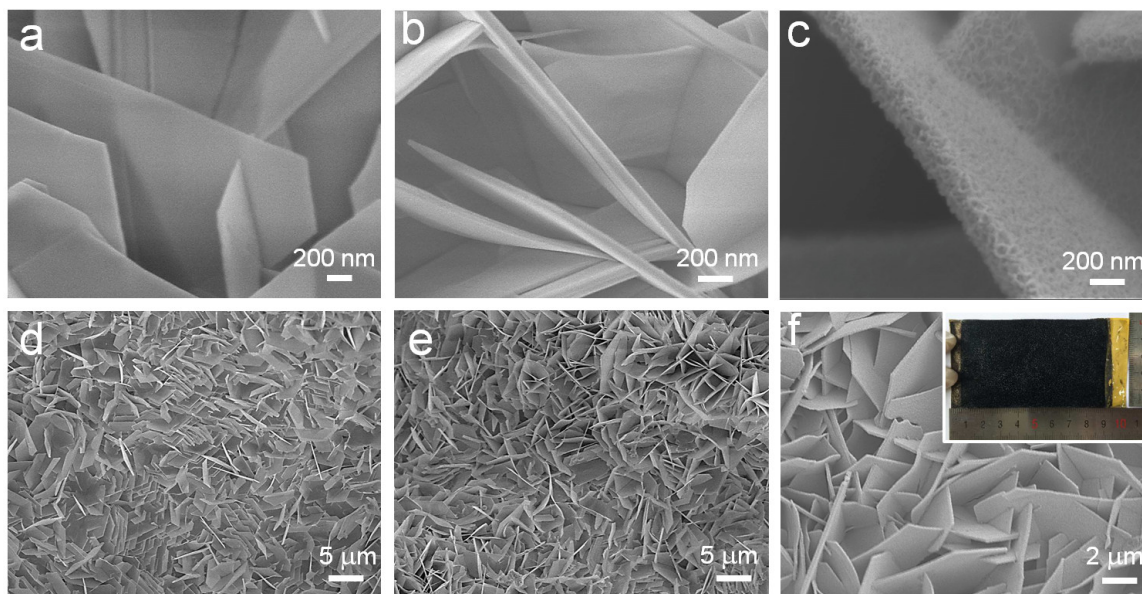


**Figure 2.** SEM images of (**a**,**d**) FNC, (**b**,**e**) $TiO_2$@FNC and (**c**,**f**) $TiO_2$@FNS arrays. The inset of (**f**) is the optical photograph for large-scale fabricated $TiO_2$@FNS electrode.

Transmission electron microscope (TEM) images provide us with further insight into the structure of FNC and $TiO_2$@FNS at the nanoscale. The FNC exhibits a nanosheet structure with a smooth surface (Figure 3a). Meanwhile, the measured interplanar d-spacing is ~0.37 nm (Figure 3b), which is in good agreement with the (006) plane of $Fe_2Ni_2CO_3(OH)_8$ phase. In the selected area electron diffraction (SAED) pattern (Figure 3c), obvious diffraction spots can be observed, matching well with the (003), (006) and (012) planes of $Fe_2Ni_2CO_3(OH)_8$ [25].

As for $TiO_2$@FNS arrays, the internal $TiO_2$ core is homogeneously coated by the cross-linked FNS nanoflakes (Figure 3d). A clear interplanar d-spacing of ~0.28 nm is observed in the HRTEM image (Figure 3e), corresponding to (311) plane of $FeNi_2S_4$ phase. Moreover, the diffraction rings in Figure 3f reveals the amorphous and polycrystal property of FNS, respectively corresponding to the (111), (311) and (400) facets of $FeNi_2S_4$ [26]. In addition, energy dispersive X-ray (EDS) mapping images (Figure 3g) demonstrate the uniform distribution of Fe, Ni, S, O and Ti elements in the $TiO_2$@FNS core-branch arrays.

X-ray diffraction (XRD) and X-ray photoelectron spectroscopy (XPS) were performed to confirm the phase and composition of $TiO_2$@FNS branch nanoflake arrays. As shown in Figure 4a, apart from the peaks of Ni foam, other diffraction peaks match well with $Fe_2Ni_2CO_3(OH)_8$ phase (JCPDS 49-0188) [27]. After ALD and sulfurization process, new diffraction peaks correspond to $FeNi_2S_4$ phase (JCPDS 47-1740) [28], revealing the successful preparation of FNS. Note that no diffraction peaks of $TiO_2$ can be observed due to its amorphous feature. The composition of FNS branch arrays is further verified by XPS results. Figure 4b exhibits the high-resolution Ni 2p spectra of the $TiO_2$@FNS branch nanoflake arrays. In addition to two shake-up satellite peaks, the peaks located at 873.48 and 856.08 eV belong to Ni $2p_{1/2}$ and Ni $2p_{3/2}$, respectively. Moreover, two smaller peaks are indexed to 853.28 and 872.28 eV, suggesting the co-existence of $Ni^{2+}/Ni^{3+}$ [29]. According to Gaussian fitting, the high-resolution Fe 2p spectra shows four peaks (Figure 4c), in which the peaks at 711.08 eV and 724.48 eV are in good agreement with the $Fe^{2+}$ [30], while the peaks indexed to 713.18 and 726.68 eV match well with the $Fe^{3+}$ species[31]. As for the S 2p spectra (Figure 4d), two

peaks at 162.74 eV (S $2p_{1/2}$) and 161.68 eV (S $2p_{3/2}$) are observed, being consistent with the $S^{2-}$ [29]. In addition, the O 1s and Ti 2p spectra are detected in the TiO$_2$@FNS branch nanoflake arrays. Two core levels at 530.78 and 531.59 eV match well with Ti-O bond and O-H bond, respectively (Figure 4e) [32].Ti $2p_{3/2}$ (458.03 eV) and Ti $2p_{1/2}$ (463.73 eV) characteristic peaks in Figure 4f further confirm the existence of TiO$_2$ [33]. All these results mutually prove the successful fabrication of TiO$_2$@FNS arrays.
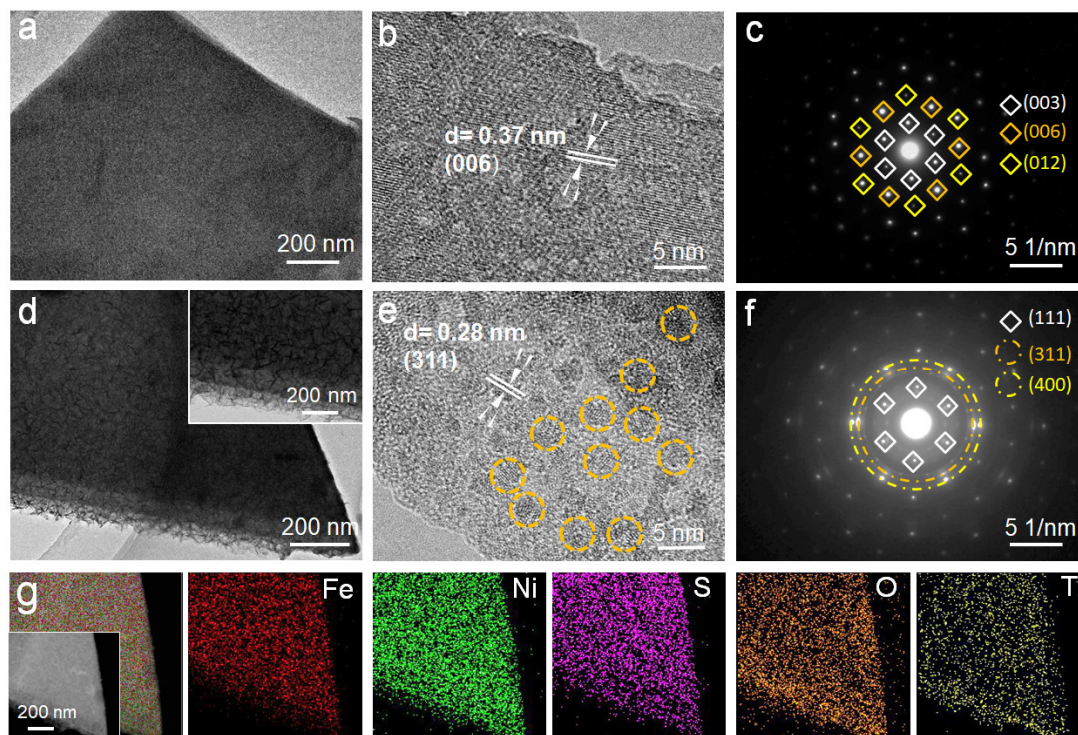


**Figure 3.** (**a**) TEM image, (**b**) HRTEM image and (**c**) SAED pattern of FNC nanosheet; (**d**) TEM image, (**e**) HRTEM image, (**f**) SAED pattern and (**g**) EDS mapping images of TiO$_2$@FNS core-branch nanosheet.
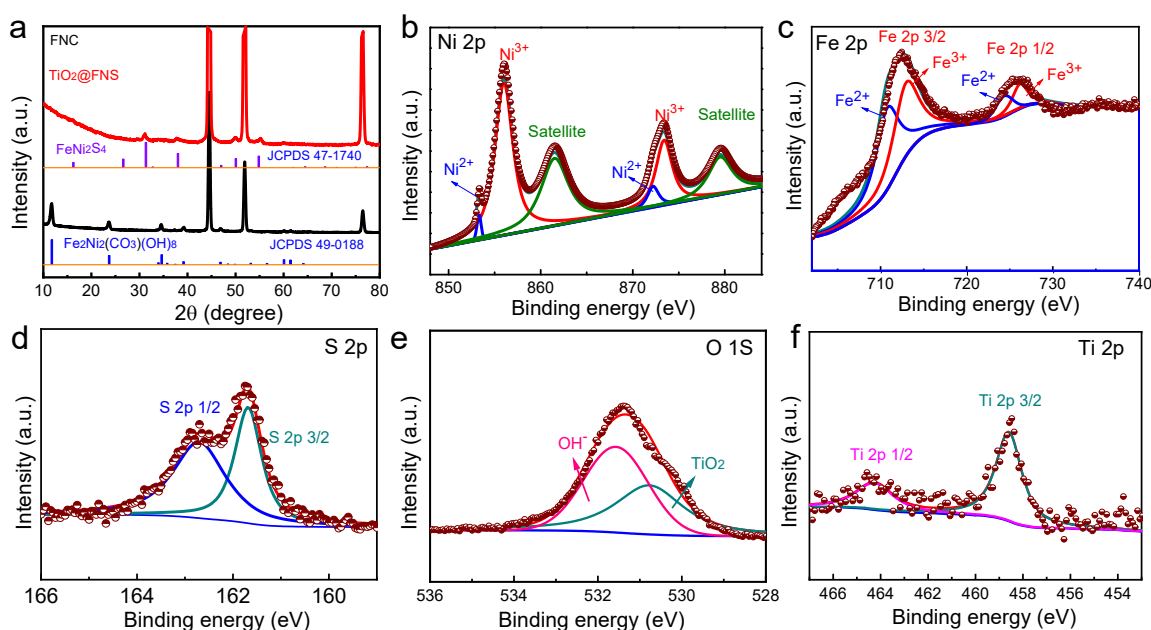


**Figure 4.** (**a**) XRD pattern of FNC and TiO$_2$@FNS arrays. XPS spectra of TiO$_2$@FNS arrays: (**b**) Ni 2p, (**c**) Fe 2p, (**d**) S 2p, (**e**) O 1s, and (**f**) Ti 2p.

## 2.2. Electrochemical Performance Analyses

The HER activity of TiO$_2$@FNS was assessed in a three-electrode cell with 1 M KOH solution as the electrolyte. FNC and FNS on Ni foam were also directly used as the test electrodes to evaluate their HER electrocatalytic performances for comparison.

As exhibited in Figure 5a, TiO$_2$ shows a negligible HER activity. Moreover, compared with FNC, FNS and TiO$_2$@NS counterparts, our fabricated TiO$_2$@FNS sample displays the best HER performance with the lowest overpotential of 97 mV at 10 mA cm$^{-2}$. The effective electrochemical active surface areas (ECSA) of all samples were estimated by testing the double-layer capacitance (Cdl) based on the CV results at different scan rates. As shown in Figure 5b, the ECSA value is deemed to the half of the slope value. The TiO$_2$@FNS branch nanoflake electrode possesses an ECAS value of 51 mF cm$^{-2}$, much larger than the TiO$_2$ (4 mF cm$^{-2}$), FNC (14 mF cm$^{-2}$), FNS (31 mF cm$^{-2}$) and TiO$_2$@NS (42 mF cm$^{-2}$) [34] electrodes. Moreover, even compared with other reported HER electrocatalysts (CoP [35], NiS$_2$ [36], Co$_9$S$_8$ [37], Ni$_3$S$_2$ [38], CoS [39], MoSe$_2$ [40], Mo$_2$C [41] and Ni$_{0.7}$Fe$_{0.3}$S$_2$ [42]), our TiO$_2$@FNS core-branch arrays still exhibit a superior HER property (Figure 5c). Low charge-transfer resistance is a characteristic of an effective electrocatalyst, especially a C-free electrocatalyst. Thus, electrochemical impendence spectroscopy was conducted to obtain charge-transfer data. Obviously, the TiO$_2$@FNS electrode shows a smaller semicircular diameter than TiO$_2$, FNC, FNS, and TiO$_2$@NS samples (Figure 5d), suggesting that the introduction of TiO$_2$ contributes to the optimized electronic structure. In addition, the TiO$_2$@FNS core-branch electrode shows a remarkable long-term durability with no obvious fluctuation of overpotential and maintains a current density of 10 mA cm$^{-2}$ in the HER over a 10 h durability test (Figure 5e). Furthermore, TiO$_2$@FNS electrode still remains intact core-branch structure and intrinsic element composition after a 10 h test (Figure S1), demonstrating its high structural stability. Such excellent HER activity and structural stability of TiO$_2$@FNS branch nanoflake arrays are owing to the increased specific surface area and the introduced TiO$_2$ coating.
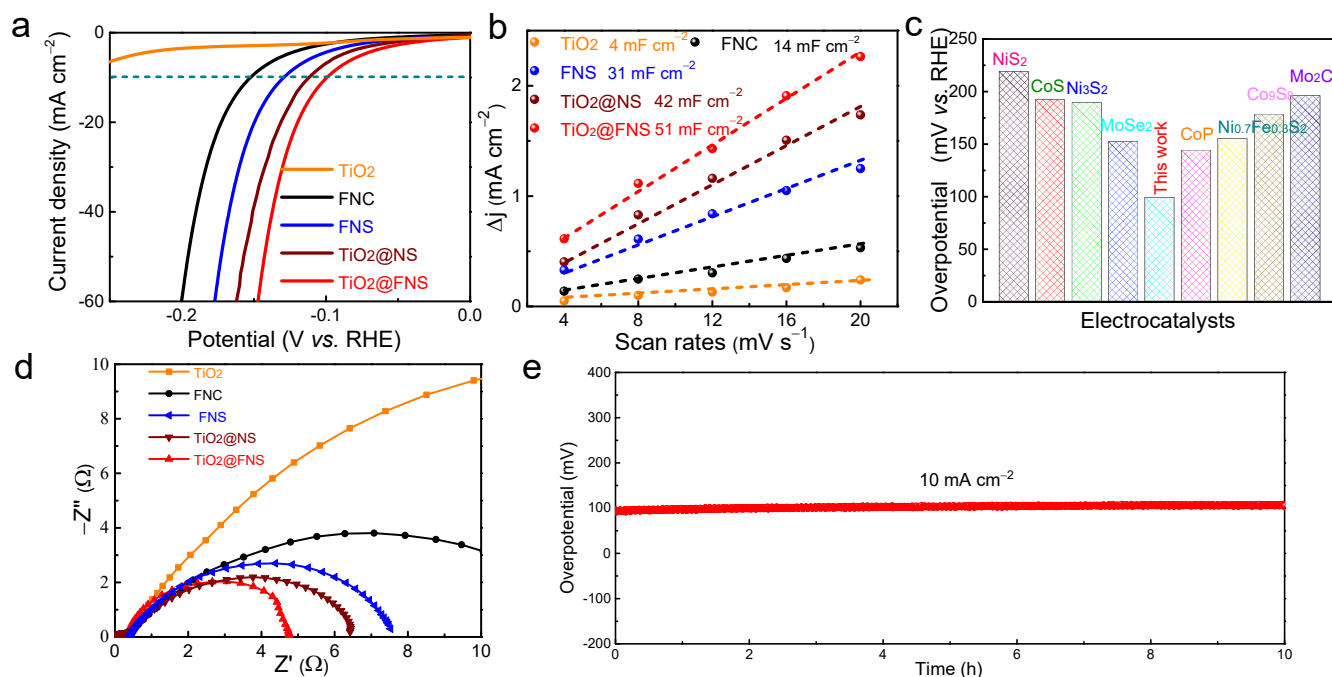


**Figure 5.** (**a**) LSV curves and (**b**) the ratio of current density with various scan rates of TiO$_2$, FNC, FNS, TiO$_2$@NS and TiO$_2$@FNS samples. (**c**) HER performance comparison of different materials. (**d**) EIS of TiO$_2$, FNC, FNS, TiO$_2$@NS and TiO$_2$@FNS samples. (**e**) Cycling performance of TiO$_2$@FNS electrode at 10 mA cm$^{-2}$.

## 2.3. DFT Calculation

In order to obtain a deep understanding of superior HER activity for $TiO_2$@FNS, we use the DFT calculation to investigate its water adsorption property and H proton adsorption/desorption property. It is well known that the adsorption energy of water molecules and H protons are the critical descriptors for HER in alkaline electrolyte. Figure 6a,b shows the water and H proton adsorption model of $FeNi_2S_4$, respectively. As shown in Figure 6c, the $FeNi_2S_4$ exhibits a water molecule adsorption energy of $-0.13$ eV, larger than the monometallic $Ni_3S_2$ ($-0.09$ eV). In addition, compared with monometallic $Ni_3S_2$ (1.01 eV), the $FeNi_2S_4$ also possesses a smaller H proton adsorption energy of 0.82 eV (Figure 6d). These results reveal that bimetallic $FeNi_2S_4$ can promote the dissociation of water molecule and the desorption of H, thereby displaying a higher intrinsic HER catalytic activity.
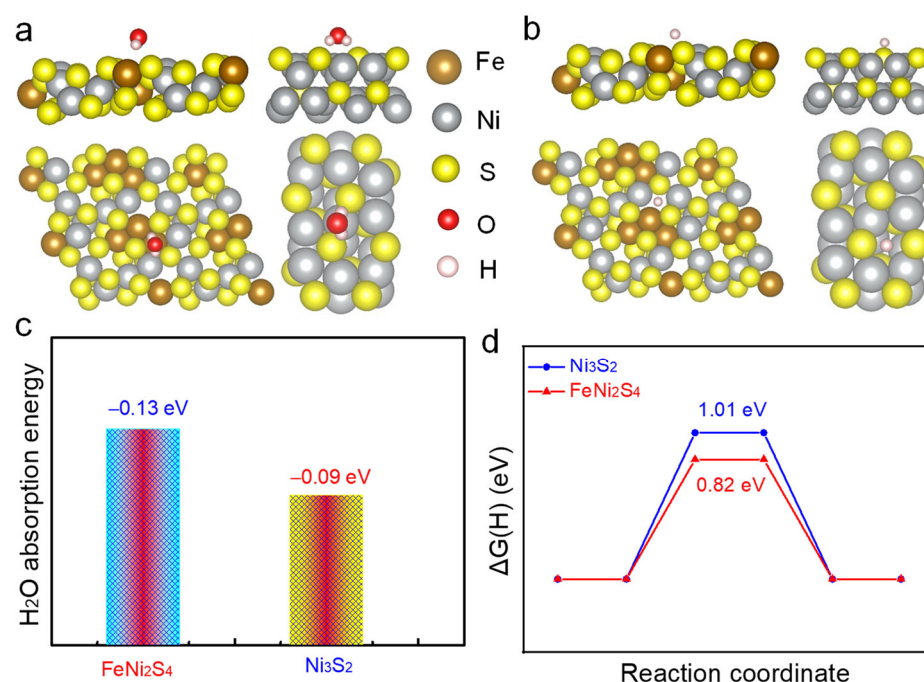


**Figure 6.** (**a**) Water molecule adsorption and (**b**) H proton adsorption model of $FeNi_2S_4$ (311) plane. (**c**) Water molecule adsorption energy and (**d**) H proton adsorption energy comparison results of $FeNi_2S_4$ and $Ni_3S_2$.

## 3. Materials and Methods

### 3.1. Synthesis of TiO₂@FNS Arrays on Ni Foam

First, the growth precursor of $Fe_2Ni_2CO_3(OH)_8$ (FNC) nanosheet arrays were prepared by a simple hydrothermal method. Here, 3 mmol $Fe(NO_3)_2$, 6 mmol $NH_4F$ and 15 mmol urea were dissolved in 80 mL deionized water to form a homogeneous solution. Moreover, the Ni foam was used as the substrate and Ni source. Then, the above solution and Ni foam were transferred into a Teflon-linked steel autoclave and kept at 120 °C for 8 h to form FNC nanosheet arrays. Then the obtained FNC nanosheet arrays were placed in the ALD reactor (ALD PICOSUN P-300F, Espoo, Finland) with $TiCl_4$ and $H_2O$ as the titanium source and O source, respectively. The $TiO_2$ was deposited at 120 °C for 140 cycles. Argon was used as the carrier gas. Then, the obtained $TiO_2$@FNC film underwent a low-temperature sulfurization process by immersing into 0.1 M $Na_2S$ solution at 90 °C for 12 h to form the final $TiO_2$@FNS branch nanoflake arrays. For comparison, the pure FNS nanosheet arrays were fabricated by the same sulfurization procedure as above without $TiO_2$ layer.

### 3.2. Characterization

The morphology and microstructure of all the samples were characterized by field emission scanning electron microscope (FESEM, Hitachi SU8010, Tokyo, Japan) and trans-

mission electron microscope (TEM, JEOL 2100F, Tokyo, Japan). X-ray diffraction (XRD) reactor with Cu Kα radiation (Rigaku D/Max-2550, Shimadzu, Kyoto, Japan) was used to monitor the phase of all the samples. X-ray photoelectron spectroscopy was also performed to study the valence of samples by using an Al Kα source of 1486.6 eV (Thermo Fisher Scientific, Waltham, MA, USA).

### 3.3. Electrochemical Measurements

All samples were used as the test electrode directly and the electrochemical measurements were conducted in a three-electrode configuration at room temperature with Pt foil and saturated calomel electrode (SCE) as the contrast and reference electrode, respectively. One (1) M KOH solution was used as the electrolyte. The E(SCE) was turned into E(RHE) based on the following equation: E(RHE) = E(SCE) + 1.0714 V. Electrodes were first scanned by CV test at a scan rate of 100 mV s$^{-1}$ over 10 cycles to stabilize the current. Linear sweep voltammetry (LSV) tests were tested at a scan rate of 1 mV s$^{-1}$. Tafel plots were obtained from LSV curves. The stability test was performed at a constant current density of 10 mA cm$^{-2}$. The above test results were obtained by iR-compensation. The effective electrochemical active surface area (ECSA) value was equal to half of the slope value, which was obtained according to a function relationship between the measured current and scan rates.

### 3.4. Computational Methods and Models

Density functional theory (DFT) calculations were performed using the quantum espresso (QE) [43,44] based on the pseudopotential plane wave (PPW) method. The Perdew-Bueke-Ernzerhof (PBE) functional [45] was used to describe exchange-correlation effects of electrons. We have chosen the projected augmented wave (PAW) potentials [46,47] to describe the ionic cores and take valence electrons into account using a plane wave basis set with a kinetic energy cutoff of 500 eV.

## 4. Conclusions

In summary, we have demonstrated a simple approach using ALD and sulfurization to fabricate a novel TiO$_2$@FNS branch nanoflake arrays on a large scale, in which the TiO$_2$ coating provides a key for enhancing the HER performance of integrated electrode. Due to the increased specific surface area and improved structural stability, the obtained TiO$_2$@FNS branch nanoflake arrays exhibit noticeable HER activity in alkaline medium with a low overpotentials (97 mV at 10 mA cm$^{-2}$), much superior to FNS and other reported electrocatalysts. We believe our work will give valuable insights for developing superior HER catalysts and beyond.

## References

1. Li, C.; Wang, Z.; Liu, M.; Wang, E.; Wang, B.; Xu, L.; Jiang, K.; Fan, S.; Sun, Y.; Li, J.; et al. Ultrafast self-heating synthesis of robust heterogeneous nanocarbides for high current density hydrogen evolution reaction. *Nat. Commun.* **2022**, *13*, 3338. [CrossRef] [PubMed]
2. Yang, X.; Cheng, J.; Yang, X.; Xu, Y.; Sun, W.; Zhou, J. Facet-tunable coral-like Mo2C catalyst for electrocatalytic hydrogen evolution reaction. *Chem. Eng. J.* **2023**, *451*, 138977. [CrossRef]
3. Zhao, G.; Rui, K.; Dou, S.X.; Sun, W. Heterostructures for Electrochemical Hydrogen Evolution Reaction: A Review. *Adv. Funct. Mater.* **2018**, *28*, 1803291. [CrossRef]
4. Che, S.; Ta, N.; Yang, F.; Yang, Y.; Li, Y. I Interfacial electronic engineering of NiSe–anchored Ni–N–C composite electrocatalyst for efficient hydrogen evolution. *Catalysts* **2022**, *12*, 1525. [CrossRef]
5. Zhou, Q.; Bian, Q.; Liao, L.; Yu, F.; Li, D.; Tang, D.; Zhou, H. In situ electrochemical dehydrogenation of ultrathin Co(OH)2 nanosheets for enhanced hydrogen evolution. *Chin. Chem. Lett.* **2023**, *34*, 107248. [CrossRef]
6. Tong, Y.; Liu, J.; Wang, L.; Su, B.-J.; Wu, K.-H.; Juang, J.-Y.; Hou, F.; Yin, L.; Dou, S.; Liu, J.; et al. Carbon-Shielded Single-Atom Alloy Material Family for Multi-Functional Electrocatalysis. *Adv. Funct. Mater.* **2022**, *32*, 2205654. [CrossRef]
7. Karmodak, N.; Andreussi, O. Catalytic Activity and Stability of Two-Dimensional Materials for the Hydrogen Evolution Reaction. *ACS Energy Lett.* **2020**, *5*, 885–891. [CrossRef]
8. Zeng, F.; Mebrahtu, C.; Liao, L.; Beine, A.K.; Palkovits, R. Stability and deactivation of OER electrocatalysts: A review. *J. Energy Chem.* **2022**, *69*, 301–329. [CrossRef]
9. Xu, Z.; Hao, M.; Liu, X.; Ma, J.; Wang, L.; Li, C.; Wang, W. Co(OH)2 nanoflowers decorated α-NiMoO4 nanowires as a bifunctional electrocatalyst for efficient overall water splitting. *Catalysts* **2022**, *12*, 1417; [CrossRef]
10. Li, C.; Jang, H.; Kim, M.G.; Hou, L.; Liu, X.; Cho, J. Ru-incorporated oxygen-vacancy-enriched MoO2 electrocatalysts for hydrogen evolution reaction. *Appl. Catal. B Environ.* **2022**, *307*, 121204. [CrossRef]
11. Ye, J.; Zang, Y.; Wang, Q.; Zhang, Y.; Sun, D.; Zhang, L.; Wang, G.; Zheng, X.; Zhu, J. Nitrogen doped FeS2 nanoparticles for efficient and stable hydrogen evolution reaction. *J. Energy Chem.* **2020**, *56*, 283–289. [CrossRef]
12. Liao, L.; Zhao, Y.; Zhou, H.; Li, D.; Qi, Y.; Zhang, Y.; Sun, Y.; Zhou, Q.; Yu, F. Edge-oriented N-Doped WS2 Nanoparticles on Porous Co3N Nanosheets for Efficient Alkaline Hydrogen Evolution and Nitrogenous Nucleophile Electrooxidation. *Small* **2022**, *18*, 2203171. [CrossRef] [PubMed]
13. Zhou, H.; Wang, Y.; He, R.; Yu, F.; Sun, J.; Wang, F.; Lan, Y.; Ren, Z.; Chen, S. One-step synthesis of self-supported porous NiSe2/Ni hybrid foam: An efficient 3D electrode for hydrogen evolution reaction. *Nano Energy* **2016**, *20*, 29–36. [CrossRef]
14. Deng, S.; Yang, F.; Zhang, Q.; Zhong, Y.; Zeng, Y.; Lin, S.; Wang, X.; Lu, X.; Wang, C.-Z.; Gu, L.; et al. Phase Modulation of (1T-2H)-MoSe2/TiC-C Shell/Core Arrays via Nitrogen Doping for Highly Efficient Hydrogen Evolution Reaction. *Adv. Mater.* **2018**, *30*, 1802223. [CrossRef]
15. Zang, Y.; Yang, B.; Li, A.; Liao, C.; Chen, G.; Liu, M.; Liu, X.; Ma, R.; Zhang, N. Tuning Interfacial Active Sites over Porous Mo$_2$N-Supported Cobalt Sulfides for Efficient Hydrogen Evolution Reactions in Acid and Alkaline Electrolytes. *ACS Appl. Mater. Interfaces* **2021**, *13*, 41573–41583. [CrossRef]
16. Liu, Z.; Li, J.; Xue, S.; Zhou, S.; Qu, K.; Li, Y.; Cai, W. Pt/Mo2C heteronanosheets for superior hydrogen evolution reaction. *J. Energy Chem.* **2020**, *47*, 317–323. [CrossRef]
17. Liu, W.; Geng, P.; Li, S.; Liu, W.; Fan, D.; Lu, H.; Lu, Z.; Liu, Y. Tuning electronic configuration of WP2 nanosheet arrays via nickel doping for high-efficiency hydrogen evolution reaction. *J. Energy Chem.* **2020**, *55*, 17–24. [CrossRef]
18. Lin, L.; Sherrell, P.; Liu, Y.; Lei, W.; Zhang, S.; Zhang, H.; Wallace, G.G.; Chen, J. Engineered 2D Transition Metal Dichalcogenides— A Vision of Viable Hydrogen Evolution Reaction Catalysis. *Adv. Energy Mater.* **2020**, *10*, 1903870. [CrossRef]
19. Morozan, A.; Johnson, H.; Roiron, C.; Genay, G.; Aldakov, D.; Ghedjatti, A.; Nguyen, C.T.; Tran, P.D.; Kinge, S.; Artero, V. Nonprecious Bimetallic Iron–Molybdenum Sulfide Electrocatalysts for the Hydrogen Evolution Reaction in Proton Exchange Membrane Electrolyzers. *ACS Catal.* **2020**, *10*, 14336–14348. [CrossRef]
20. Yang, H.; Driess, M.; Menezes, P.W. Self-Supported Electrocatalysts for Practical Water Electrolysis. *Adv. Energy Mater.* **2021**, *11*, 2102074. [CrossRef]
21. Sivanantham, A.; Ganesan, P.; Shanmugam, S. Hierarchical NiCo$_2$S$_4$ Nanowire Arrays Supported on Ni Foam: An Efficient and Durable Bifunctional Electrocatalyst for Oxygen and Hydrogen Evolution Reactions. *Adv. Funct. Mater.* **2016**, *26*, 4661–4672. [CrossRef]
22. Zhao, Y.; Mavrokefalos, C.K.; Zhang, P.; Erni, R.; Li, J.; Triana, C.A.; Patzke, G.R. Self-Templating Strategies for Transition Metal Sulfide Nanoboxes as Robust Bifunctional Electrocatalysts. *Chem. Mater.* **2020**, *32*, 1371–1383. [CrossRef]
23. Su, H.; Song, S.; Gao, Y.; Li, N.; Fu, Y.; Ge, L.; Song, W.; Liu, J.; Ma, T. In Situ Electronic Redistribution Tuning of NiCo2S4 Nanosheets for Enhanced Electrocatalysis. *Adv. Funct. Mater.* **2022**, *32*, 2109731. [CrossRef]
24. Jadhav, H.S.; Roy, A.; Thorat, G.M.; Chung, W.-J.; Gil Seo, J. Hierarchical free-standing networks of MnCo2S4 as efficient Electrocatalyst for oxygen evolution reaction. *J. Ind. Eng. Chem.* **2018**, *71*, 452–459. [CrossRef]
25. Li, L.; Dai, Y.; Xu, Q.; Zhang, B.; Zhang, F.; You, Y.; Ma, D.; Li, S.-S.; Zhang, Y.-X. Interlayer expanded nickel-iron layered double hydroxide by intercalation with sodium dodecyl sulfate for enhanced oxygen evolution reaction. *J. Alloy. Compd.* **2021**, *882*, 160752. [CrossRef]

26. Liu, Y.; Li, Y.; Srinivas, K.; Wang, M.; Liu, D.; Chen, X.; Wang, B.; Wang, S.; Chen, Y. Heterogeneous FeNi2S4/Ni3S4 nanoparticles embedded CNT networks for efficient and stable water oxidation. *Journal Alloys Compounds* **2022**, *914*, 165327. [CrossRef]

27. Ren, L.; Wang, C.; Li, W.; Dong, R.; Sun, H.; Liu, N.; Geng, B. Heterostructural NiFe-LDH@Ni$_3$S$_2$ nanosheet arrays as an efficient electrocatalyst for overall water splitting. *Electrochim. Acta* **2019**, *318*, 42–50. [CrossRef]

28. Jiang, J.; Zhang, Y.-J.; Zhu, X.-J.; Lu, S.; Long, L.-L.; Chen, J.-J. Nanostructured metallic FeNi2S4 with reconstruction to generate FeNi-based oxide as a highly-efficient oxygen evolution electrocatalyst. *Nano Energy* **2020**, *81*, 105619. [CrossRef]

29. Wu, Y.; Li, Y.; Yuan, M.; Hao, H.; San, X.; Lv, Z.; Xu, L.; Wei, B. Operando capturing of surface self-reconstruction of Ni3S2/FeNi2S4 hybrid nanosheet array for overall water splitting. *Chem. Eng. J.* **2022**, *427*, 131944. [CrossRef]

30. Yu, F.; Zhou, H.; Zhu, Z.; Sun, J.; He, R.; Bao, J.; Chen, S.; Ren, Z. Three-Dimensional Nanoporous Iron Nitride Film as an Efficient Electrocatalyst for Water Oxidation. *ACS Catal.* **2017**, *7*, 2052–2057. [CrossRef]

31. Liu, C.; Jia, D.; Hao, Q.; Zheng, X.; Li, Y.; Tang, C.; Liu, H.; Zhang, J.; Zheng, X. P-Doped Iron–Nickel Sulfide Nanosheet Arrays for Highly Efficient Overall Water Splitting. *ACS Appl. Mater. Interfaces* **2019**, *11*, 27667–27676. [CrossRef] [PubMed]

32. Ma, B.; Guan, P.-Y.; Li, Q.-Y.; Zhang, M.; Zang, S.-Q. MOF-Derived Flower-like MoS$_2$@TiO$_2$ Nanohybrids with Enhanced Activity for Hydrogen Evolution. *ACS Appl. Mater. Interfaces* **2016**, *8*, 26794–26800. [CrossRef] [PubMed]

33. Gao, S.; Zavabeti, A.; Wang, B.; Ren, R.; Yang, C.; Liu, Z.; Wang, Y. Nickel Phosphides Electrodeposited on TiO$_2$ Nanotube Arrays as Electrocatalysts for Hydrogen Evolution. *ACS Appl. Nano Mater.* **2021**, *4*, 4542–4551. [CrossRef]

34. Deng, S.; Zhang, K.; Xie, D.; Zhang, Y.; Zhang, Y.; Wang, Y.; Wu, J.; Wang, X.; Fan, H.J.; Xia, X.; et al. High-Index-Faceted Ni3S2 Branch Arrays as Bifunctional Electrocatalysts for Efficient Water Splitting. *Nano-Micro Lett.* **2019**, *11*, 12. [CrossRef]

35. Li, J.; Zou, S.; Liu, X.; Lu, Y.; Dong, D. Electronic Modulation of CoP by Ce Doping as Highly Efficient Electrocatalysts for Water Splitting. *ACS Sustain. Chem. Eng.* **2020**, *8*, 10009–10016. [CrossRef]

36. Tian, T.; Huang, L.; Ai, L.; Jiang, J. Surface anion-rich NiS$_2$ hollow microspheres derived from metal–organic frameworks as a robust electrocatalyst for the hydrogen evolution reaction. *J. Mater. Chem. A* **2017**, *5*, 20985–20992. [CrossRef]

37. Yang, Y.; Yuan, M.; Li, H.; Sun, G.; Ma, S. Controllable synthesis of ultrathin Co9S8 nanosheets as a highly efficient electrocatalyst for overall water splitting. *Electrochim. Acta* **2018**, *281*, 198–207. [CrossRef]

38. Li, L.; Sun, C.; Shang, B.; Li, Q.; Lei, J.; Li, N.; Pan, F. Tailoring the facets of Ni$_3$S$_2$ as a bifunctional electrocatalyst for high-performance overall water-splitting. *J. Mater. Chem. A* **2019**, *7*, 18003–18011. [CrossRef]

39. Li, N.; Liu, X.; Li, G.-D.; Wu, Y.; Gao, R.; Zou, X. Vertically grown CoS nanosheets on carbon cloth as efficient hydrogen evolution electrocatalysts. *Int. J. Hydrogen Energy* **2017**, *42*, 9914–9921. [CrossRef]

40. Yin, Y.; Zhang, Y.; Gao, T.; Yao, T.; Zhang, X.; Han, J.; Wang, X.; Zhang, Z.; Xu, P.; Zhang, P.; et al. Synergistic Phase and Disorder Engineering in [1]T-MoSe$_2$ Nanosheets for Enhanced Hydrogen-Evolution Reaction. *Adv. Mater.* **2017**, *29*, 1700311. [CrossRef]

41. Sun, J.; Liu, J.; Chen, H.; Han, X.; Wu, Y.; He, J.; Han, C.; Yang, G.; Shan, Y. Strongly coupled Mo$_2$C and Ni nanoparticles with in-situ formed interfaces encapsulated by porous carbon nanofibers for efficient hydrogen evolution reaction under alkaline conditions. *J. Colloid Interface Sci.* **2019**, *558*, 100–105. [CrossRef]

42. Yu, J.; Cheng, G.; Luo, W. Ternary nickel–iron sulfide microflowers as a robust electrocatalyst for bifunctional water splitting. *J. Mater. Chem. A* **2017**, *5*, 15838–15844. [CrossRef]

43. Giannozzi, P.; Baroni, S.; Bonini, N.; Calandra, M.; Car, R.; Cavazzoni, C.; Ceresoli, D.; Chiarotti, G.L.; Cococcioni, M.; Dabo, I.; et al. QUANTUM ESPRESSO: A modular and open-source software project for quantum simulations of materials. *J. Phys. Condens. Matter* **2009**, *21*, 395502. [CrossRef] [PubMed]

44. Giannozzi, P.; Andreussi, O.; Brumme, T.; Bunau, O.; Nardelli, M.B.; Calandra, M.; Car, R.; Cavazzoni, C.; Ceresoli, D.; Cococcioni, M.; et al. Advanced capabilities for materials modelling with Quantum ESPRESSO. *J. Phys. Condens. Matter* **2017**, *29*, 465901. [CrossRef] [PubMed]

45. Perdew, J.P.; Burke, K.; Ernzerhof, M. Generalized gradient approximation made simple. *Phys. Rev. Lett.* **1996**, *77*, 3865. [CrossRef] [PubMed]

46. Blöchl, P.E.; Jepsen, O.; Andersen, O.K. Improved tetrahedron method for Brillouin-zone integrations. *Phys. Rev. B* **1994**, *49*, 16223–16233. [CrossRef] [PubMed]

47. Kresse, G.; Joubert, D. From ultrasoft pseudopotentials to the projector augmented-wave method. *Phys. Rev. B* **1999**, *59*, 1758–1775. [CrossRef]